

Wavelets and Notch Filtering

Innovative Techniques for Mitigating RF Interference



© Shutterstock/Stockphoto.com/Dimitar Martirov

As interest in use of GNSS for safety critical applications gains momentum, interference concerns abound. Pulsed interference and continuous wave signals can degrade the reception of GNSS signals. The authors present emerging concepts for detecting and mitigating interference by means of digital processing techniques applied in the receiver.

MATTEO PAONNI, JAEGYU JANG, AND
BERND EISSFELLER
UNIVERSITY FAF MUNICH, GERMANY

STEFAN WALLNER, JOSÉ ÁNGEL
ÁVILA-RODRÍGUEZ, JARON SAMSON, AND
FRANCISCO AMARILLO FERNÁNDEZ
ESA/ESTEC, THE NETHERLANDS

The use of GNSS for safety critical applications is gaining interest, particularly amongst aviation users, who probably have the most demanding requirements. The GNSS frequency band containing the Galileo E5 and GPS L5 signals is designated as an aeronautical radio navigation service (ARNS) band, which enjoys legal protection from other services not allocated to this frequency on a primary basis.

However, GNSSes do not hold exclusive rights to this frequency, and its use of the frequency on a primary basis may

expose a GNSS signal to potential interference from other services that enjoy similar emission rights, affecting performance in safety critical applications.

These other services include pulsed interference originating from systems such as distance measuring equipment (DME), Tactical Air Navigation (TACAN) signals, and the Joint Tactical Information Distribution System (JTIDS), as well as military radars that may cause significant service degradation. Moreover, in addition to the severe effects on the E5/L5 band by induced interference, the situation becomes even more problematical when these signals are used in conjunction with the Galileo E6 frequency band.

Not only pulsed interference, but also other RF transmissions such as continuous wave (CW) signals can degrade the reception of GNSS signals. An example of such interference occurs due to the

harmonics originating from the European digital video broadcast terrestrial (DVB-T) service, which can appear in RNSS frequency bands.

Interference can be mitigated through various means. On the hardware side, specialized instrumentation such as choke rings or active beam-forming antennas, suppress interference and improve the reception of line-of-sight satellite signals. Special RF front-end architectures make use of pulse blanker and/or automatic gain control (AGC) to reduce RFI. With respect to a GNSS receiver's digital signal processor (DSP), performance degradation due to interference can be treated in the receiver's software, using interference mitigation algorithms.

In this column, we will focus on the DSP solutions, although we need to emphasize that in order to achieve the best results, all three elements of a gener-

ic GNSS receiver antenna, RF front-end, and DSP — must be considered, while measures taken for any individual element need to be coordinated with the others.

Interference Mitigation by Means of Wavelet

Pulse blanking is the most common approach to suppress pulsed interference. However, some traditional pulse blanking designs are based on monitoring the automatic gain control (AGC) within the receiver's front-end and activating the blanking at instances when an abrupt and significant increase of the AGC is reported. Due to the limited dynamics of the AGC, pulse blanking suffers is less effective in cases where high pulse repetition frequencies occur.

The wavelet based technique described in detail by C. Burrus *et alia* in the publication cited in the Additional Resources section near the end of this article is not based on AGC techniques. Thus, it is not only suited for high power pulses but also for medium to low power pulses, as we will demonstrate later on. Further benefits of the wavelet approach to interference mitigation for pulsed interference are explained in the article by E. Anyaegbu *et alia* (see Additional Resources) in the frame of GNSS signal processing.

The traditional Fourier series and fast Fourier transformation (FFT) are based on sinusoidal functions with infinite support. Although applying this transformation gives complete insight into the signal's frequency evolution, it removes all time-dependent information that we might want to analyze.

An analysis of pulsed interference requires both a time and frequency representation of the signal. To achieve this end, we could cut the signal into several time-dependent sections and then analyze each independently. However, we still need to determine the instant in time to cut the signal, while identifying all frequency components at a certain time instance.

In order to meet this desire, we cut the signal using a Dirac pulse and then

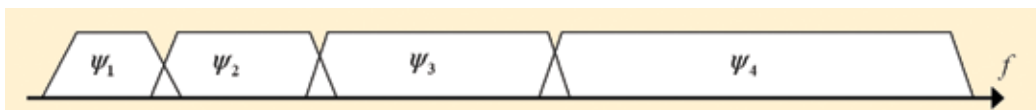


FIGURE 1 Touching wavelet spectra

transform the result to the frequency domain. The cutting of the signal corresponds to a convolution in the time domain and thus to a multiplication in the frequency domain. Finally, a Fourier transform of the Dirac pulse contains all possible frequencies and consequently the frequency information of the initial signal is smeared out to all frequencies.

This concept is an analogous to Heisenberg's uncertainty relation as — in signal processing terms — it is impossible to know the exact frequency and the exact time resolution of a signal. The key to analyzing pulsed interference can be seen in the selection of the correct cutting of the signal.

With wavelet analysis we overcome this problem by selecting the time at which to cut the signal using a flexible and scalable window function. We shift the window along the time axis for every point in time the spectrum is calculated, which can be repeated several times using slightly compressed window functions.

The final result is a time-frequency representation of the signal. In the wavelet analysis the frequency term is mostly replaced, as explained later, by a scaling operation to have a clear boundary to the Fourier transformation.

Continuous Wavelet Transformation

The continuous wavelet transformation for a time-dependent function $f(t)$ is defined as

$$\gamma(s, \tau) = \int_{-\infty}^{\infty} f(t) \psi_{s,\tau}^*(t) dt \quad (1)$$

where $*$ denotes the complex conjugation, and $\psi_{s,\tau}^*(t)$ is called the wavelet with the variables, scale, s , and translation, τ . The inverse wavelet transformation is given by

$$f(t) = \iint \psi_{s,\tau}^*(t) \gamma(s, \tau) ds d\tau \quad (2)$$

The wavelet functions are deduced from one single wavelet, the so-called

mother wavelet $\psi(t)$, by scaling and translation according to

$$\psi_{s,\tau}(t) = \frac{1}{\sqrt{s}} \psi\left(\frac{t-\tau}{s}\right) \quad (3)$$

The factor $s^{-0.5}$ guarantees energy normalization.

These formulas are not linked to a unique and single function $\psi(t)$ as with the case for the Fourier transformation. We declare functions for which a number of characteristic properties hold as “mother wavelets.” We invite interested readers to consult Burrus *et alia* for a further explanation of wavelet mother functions.

Discrete Wavelet Transformation

Working with sampled data requires the definition of a discrete Wavelet Transformation, given by

$$\Psi_{j,k}(t) = \frac{1}{\sqrt{js_0}} \psi\left(\frac{t - k\tau_0 js_0}{js_0}\right) \quad (4)$$

with integers j and k , discrete scaling steps, s_0 , and time dilations, τ_0 , but continuous with respect to the time axis, t .

Discrete wavelets require an infinite number of scalings and translations in order to be able to fully represent the original input function. Although a break-off of the wavelet series may offer a way out, the truncation error still needs to be controlled.

From the defining characteristics of a wavelet function, we suggest that Wavelet functions offer a band-pass-like spectrum, where a compression in time can also be expressed as a stretch in the frequency domain together with a shifting up to higher frequencies.

We use this characteristic to construct a series of wavelets covering the whole frequency range of our input signal, where special attention needs to be paid so that each stretched wavelet spectra touch its neighbors as shown in

Figure 1.

In practice, it is impossible to cover all spectrum of an input function down to zero. The most elegant solution resulting in applicable wavelets is to stop stretching the wavelet once the open hole is small enough and then fill it with a so-called scaling function. This function can be interpreted as a low-pass filter, described in terms of its wavelets as

$$\varphi(t) = \sum_{j,k} \gamma(j,k) \psi_{j,k}(t) \tag{5}$$

We graphically represent the use of scaling functions in **Figure 2**.

Analogously, we can also add the Wavelet and its adjacent scale function, resulting in a scaling function with a spectrum twice as wide. Mathematically, Burrus *et alia* express this as

$$\varphi(2^j t) = \sum_k h_{j+1}(k) \varphi(2^{j+1} t - k) \tag{6}$$

Equation 6 expresses one scaling function as a function of translated scaling at the next smaller scale. We describe the wavelet replaced by the scaling function in Equation (7):

$$\psi(2^j t) = \sum_k g_{j+1}(k) \varphi(2^{j+1} t - k) \tag{7}$$

Finally, we approximate the function to be transformed into its representation with wavelets, as

$$f(t) = \sum_k \lambda_{j-1}(k) \varphi(2^{j-1} t - k) + \sum_k \gamma_{j-1}(k) \psi(2^{j-1} t - k) \tag{8}$$

Under the assumptions of having orthonormal scaling functions $\varphi_{j,k}(t)$ and an orthonormal wavelet function $\psi_{j,k}(t)$, the coefficients $\lambda_{j-1}(k)$ and $\gamma_{j-1}(k)$ can be calculated as the scalar product between the scaling wavelet function and the initial function $f(t)$. We refer to the coefficients $\lambda_{j-1}(k)$ and $\gamma_{j-1}(k)$ as approximate coefficients, cA , and respectively detailed coefficients, cD , later on when we discuss the algorithmic implementation.

Pulsed Interference Mitigation by Wavelets

Now that we have defined the prerequisites for Wavelet analyses, we would like to return to our original approach to identifying and mitigating medium to low pulsed interference by means of wavelets.

Figure 3 identifies the individual steps for the wavelet-based interference mitigation, an approach that will be outlined in more detail next.

For demonstration purposes, we selected a scenario with high pulsed interference power featuring a jamming-to-signal ratio (J/S) of 51 decibels. IF samples of the signal in this scenario are represented in **Figure 4**, where the interfering pulse can clearly be detected by visual inspection. Later we will demonstrate the capabilities and the potential of interference detection by means of wavelets for low power pulses as well.

Step 1 – Discrete Wavelet Transformation. The first step towards correctly identifying pulsed interference uses a discrete wavelet transformation, with a complete manifold of potential wavelet mother functions. For the best results — that is,

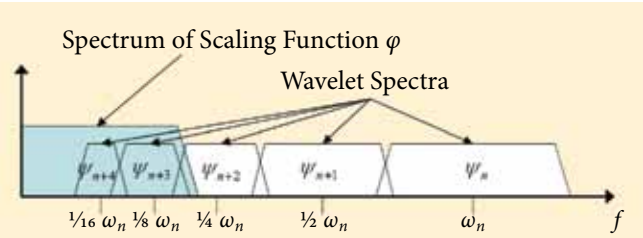


FIGURE 2 Introduction of scaling function

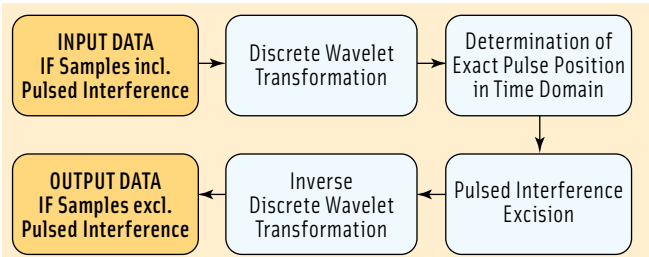


FIGURE 3 Pulsed Interference Mitigation with Wavelets

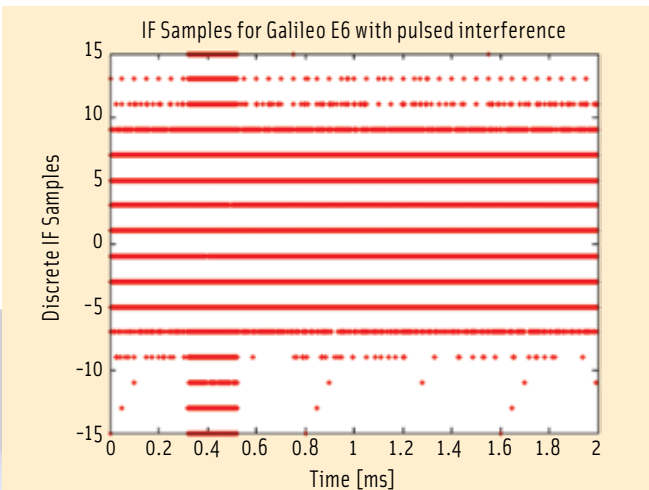


FIGURE 4 IF samples for high-power pulsed interference

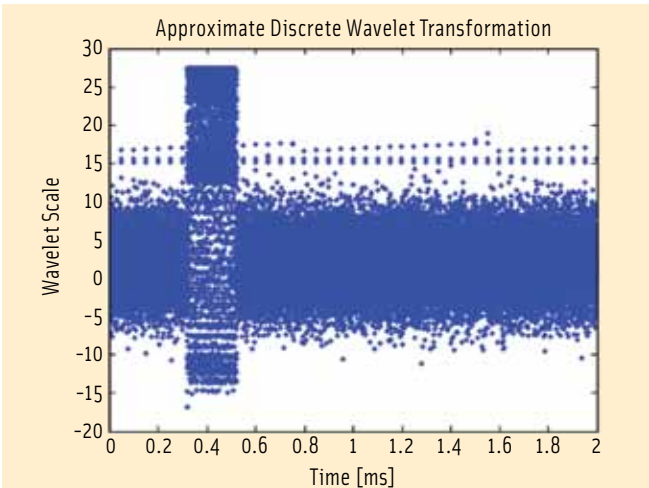


FIGURE 5 Approximate scale coefficients of the IF samples

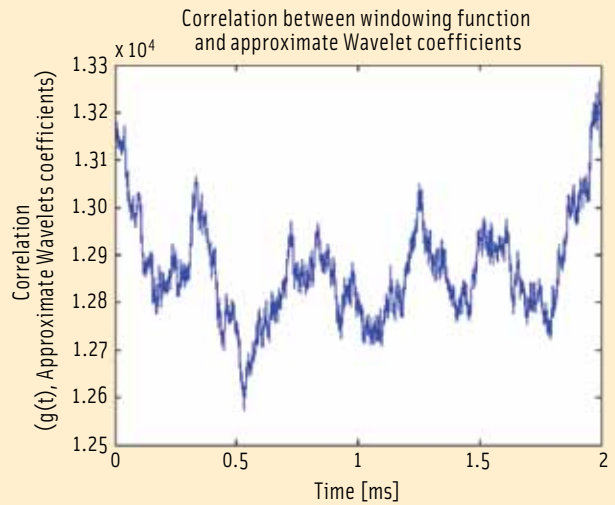
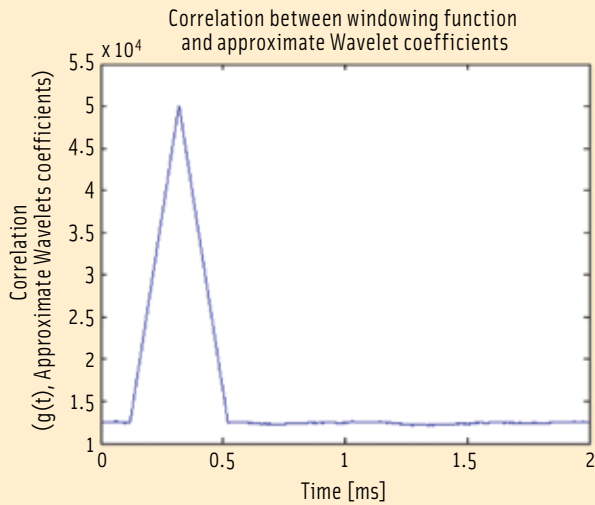


FIGURE 6 Correlation between windowing function and approximate wavelet coefficients for “pulse-present” (left) and “no pulse present” cases (right)

those yielding both the highest correlation between the pulsed interference and the wavelet, as well as the lowest correlation between the wavelet function and the GNSS plus noise signal — an optimization could be carried out. Figure 5 illustrates the approximate discrete wavelet transformation scale coefficients for the IF samples shown in Figure 4.

Step 2 – Exact Pulse Position in Time. With appropriate knowledge of the expected pulse duration, a constant windowing function $g(t)$ is generated and correlated with the approximate scale coefficients. This determines the correct time location of the pulse within the IF samples as shown in Figure 6, where an easily distinguishable local maximum is obtained in the pulse-present case.

If no pulse is present, as is the case in Figure 7, one cannot detect a maximum can be detected. In that case, we use the expression

$$\zeta = \frac{\max(CC(g(t), cA)}{\text{mean}(cA)} \quad (9)$$

as a figure of merit for pulse detection via correlation, where cA represents the approximate scale coefficients of the discrete wavelet transformation.

Step 3 – Pulsed Interference Excision. After correct identification of the pulse in the time domain, we perform a *pulse excision* by modifying the affected approximate and detailed scale coefficients, cA and cD . After comparing potential solutions by modifying the scale coefficients, the classical blanking approach still shows best performance.

Step 4 – Inverse Discrete Wavelet Transformation. In the final step, we apply an inverse discrete wavelet transformation in order to regain the original IF samples after eliminating the samples affected by pulsed interference. Figure 7 shows our results.

Low Power DME Interference Mitigation

Distance measuring equipment employs a transponder-based radio navigation technology that measures distance by timing

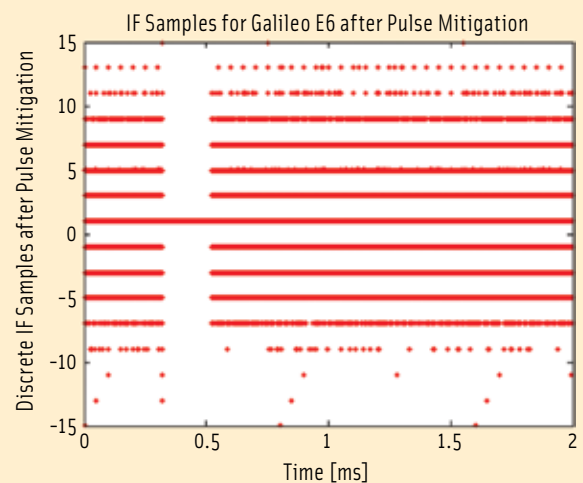


FIGURE 7 IF samples after pulse mitigation with wavelets and “wavelet based blanking”

the propagation delay of radio signals. DME pulsed interference is to be expected in the 1151–1213 megahertz frequency range when operating in X mode, thus affecting the E5/L5 band.

A typical Gaussian DME pulse pair is shown in Figure 8. While the wavelet-based interference mitigation approach has been outlined earlier for high-power pulses, here, we assess the performance of these algorithms for the case of low-power interference. We use a standard pulse interval of 12 microseconds between the two DME single pulses, while we consider a repetition rate of about 2,700 pulse pairs per second (pps) at the upper limit of the DME specifications.

The following test scenario is based on a J/S value of 18 decibels. The corresponding IF samples are presented in Figure 9.

The five DME double pulses expected in the data of are not detectable by visual inspection; however, by applying the discrete wavelet transform, we can extract the DME pulses. Figure 10 shows the approximate wavelet coefficients after wavelet

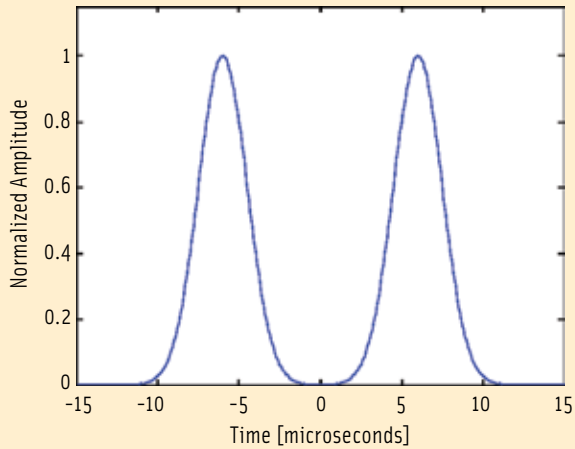


FIGURE 8 Gaussian DME pulse pair

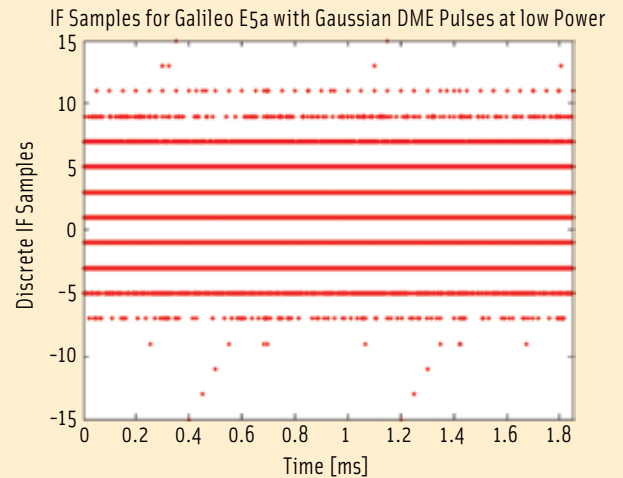


FIGURE 9 IF Samples Including Gaussian DME Pulsed Interference

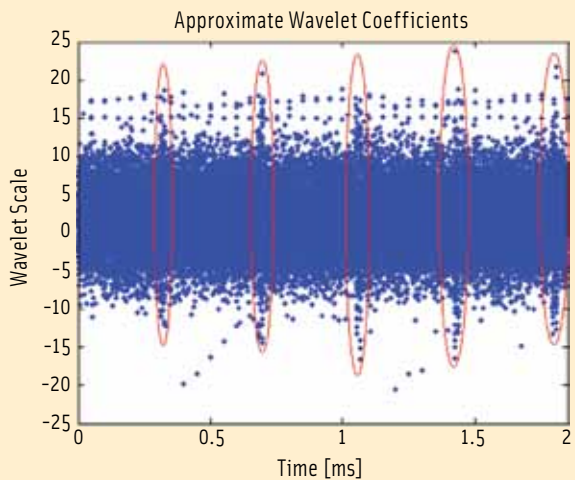


FIGURE 10 Approximate scale coefficients of the IF samples

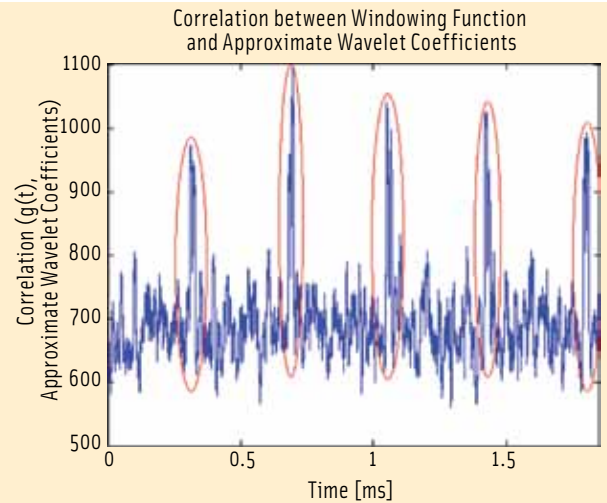


FIGURE 11 Correlation of approximate wavelet coefficients and windowing function

transform with bi-orthogonal wavelets of reconstruction order 3, and decomposition order 5 together with the expected DME pulse locations in the time domain (highlighted by the red ellipses).

The next step is to correlate the approximated wavelet coefficients, cA , with a time window function of appropriate width. As the Gaussian DME pulse shape is well known, we apply a window function $g(t)$ of 12 microseconds.

Figure 11 illustrates that the precise and explicit detection of five DME pulse pairs is now possible within the time interval of 1.85 milliseconds, as expected with pulse repetition rate of 2,700 pps. A zoomed view into the highlighted correlation values reveals the double pulse characteristic of the DME pulses. This demonstrates that even low-power

pulsed interference can be detected by applying wavelet techniques.

Performance Assessment of Wavelet-Based Interference Mitigation

Now that we have demonstrated the capability of wavelet techniques to detect interference, we will apply the mitigation approach and assess its performance. We evaluate the mitigation approach, for both the case of the high-power pulsed interference scenario as well as for low-power DME pulsed interference.

High Power Pulsed Interference. We summarize the high power pulsed interference scenario in Table 1.

We apply the wavelet mitigation algorithm and evaluate its performance by means of the IpxSR software receiv-

Desired signal	Galileo E6b/c (BPSK(5))
Coherent integration time	1 ms
Loop bandwidths	DLL: 5 Hz PLL: 10 Hz FLL: 4 Hz
RF front-end bandwidth	13 MHz (double sided)
Pulsed interference	Pulse duration: 2e-4 sec Pulse repetition rate: 300 pps J/S ratio: 51 dB

TABLE 1. Scenario characterization for high-power pulsed interference

er, developed at the Institute of Geodesy and Navigation at the University FAF Munich and described in the article by C. Stöber (Additional Resources), in terms of effective C/N_0 , delay-locked

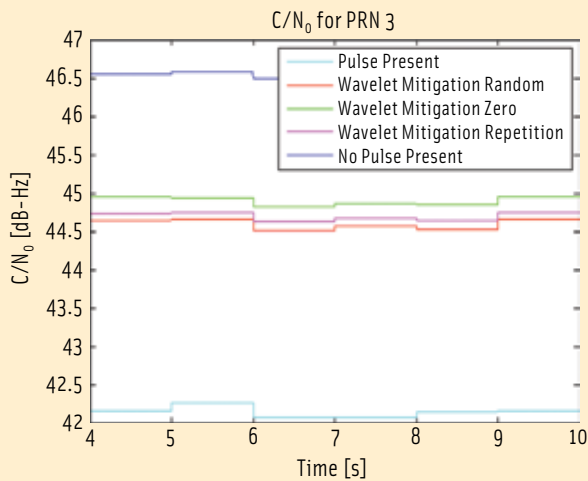


FIGURE 12 C/N_0 effective estimation for PRN 3 – High-power pulsed interference

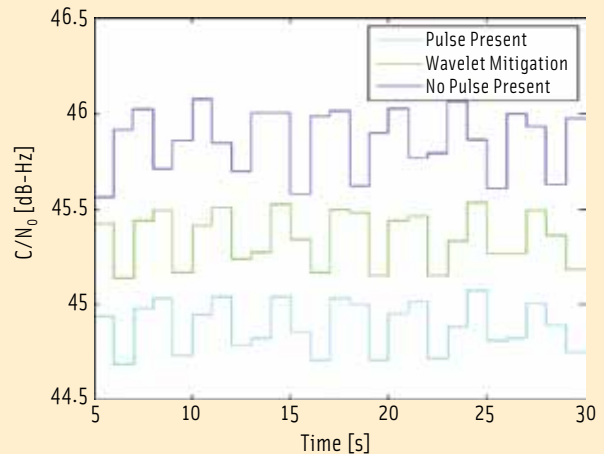


FIGURE 13 C/N_0 effective estimation for PRN 3 – Low-power DME pulsed interference

loop (DLL), phase-locked loop (PLL), and frequency-locked loop (FLL) tracking errors. The experiments were conducted on the GPS PRN 3 satellite signal, which we consider representative of any GNSS channel. After four seconds the C/N_0 estimation inside the receiver reached a steady state, as shown in Figure 12.

A significant increase in the C/N_0 of about three decibels can be observed when comparing the data set where the pulse is present (cyan) with the data sets obtained after Wavelet mitigation. As already indicated, blanking IF samples affected by interference (green) shows best performance while introducing no further noise into the system.

Table 2 reports the effect of the wavelet mitigation on the DLL, PLL, and FLL errors. All evaluation criteria yielded clear performance improvements for the high-power pulse scenario.

Low Power DME Pulsed Interference. The low-power DME pulsed interference scenario presents much more challenging mitigation problems, due to a substantially lower J/S ratio. We previously demonstrated that pulse detection using the wavelet approach is feasible. Table 3 characterizes the low power DME pulsed performance scenario.

Figure 13 illustrates the degrading effect of weak DME pulses on the effective C/N_0 — by almost one decibel in the 45.86–44.89 dB-Hz range. Applying the wavelet-based interference mitigation solution, the C/N_0 can be increased by

about 0.5 decibels compared to the pulse-present scenario. The effects of the wavelet-based interference mitigation on DLL, PLL, and FLL performance is shown only in tabular form in Table 4.

Our analyses show that wavelet-based interference mitigation can be applied to both high- and low-power pulsed interference. We have also demonstrated that the performance enhancements in the case of low power interference are not large, which was as expected.

However, the performance might change if more than one DME are simultaneously received. A measurement campaign reported by A. Steingass et alia (see Additional Resources) indicated that quite a high number of DMEs can be seen simultaneously over Europe. If interference from uncorrelated DMEs is arriving at the GNSS receiver, the performance improvements might be significantly higher than in the scenario under consideration here, with a single DME.

Wavelet-Based Interference Mitigation vs. Pulse Blanking

We compared the benefits and drawbacks of the well-established time domain pulse blanking technique with the wavelet-based approach for mitigating pulsed interference.

All analysis is based on an IpexSR software receiver with a front-end not capable of performing real-time domain blanking via AGC monitoring. A user

	No Pulse	Pulse Present	Wavelet Mitigation Zero
DLL [m]	1.4e-2	2.3e-2	1.5e-2
PLL [cycle]	3.2e-2	6.1e-3	3.8e-3
FLL [Hz]	1.7e1	3.6e1	1.8e1

TABLE 2. Standard deviation of DLL, PLL, and FLL errors

Desired signal	Galileo E5a (BPSK(10))
Coherent integration time	1 ms
Loop bandwidths	DLL: 5 Hz PLL: 10 Hz FLL: 4 Hz
RF front-end bandwidth	13 MHz (double sided)
Pulsed interference	DME double pulses • Duration of a single pulse: 3.5e-6 sec • Interval: 1.2 e-5 sec. Pulse repetition rate: 2700 pps J/S ratio: 8.4 dB

TABLE 3. Scenario characterization for low-power DME pulsed interference

	No Pulse	Pulse Present	Wavelet Mitigation Zero
DLL [m]	2.571e-1	2.607e-1	2.595e-1
PLL [cycle]	1.899e-2	2.519e-2	1.94e-2
FLL [Hz]	5.879	7.252	6.035

TABLE 4. Standard deviation of DLL, PLL, and FLL errors

sets the gain factor externally as a function of the specific antenna used. Thus,

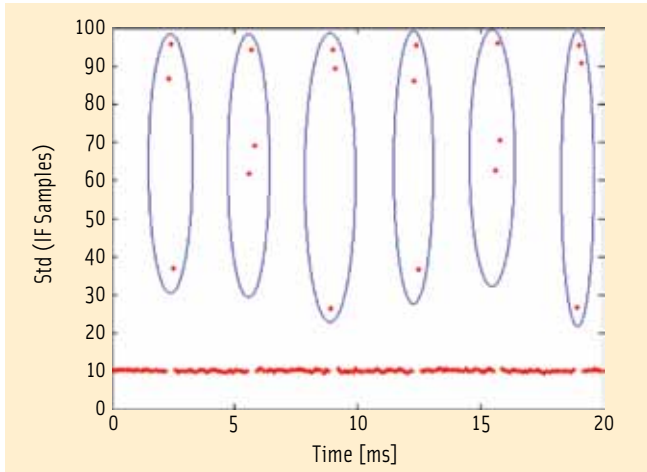


FIGURE 14 Standard deviation of the IF samples of Galileo E6 contaminated with high power, long pulsed interference.

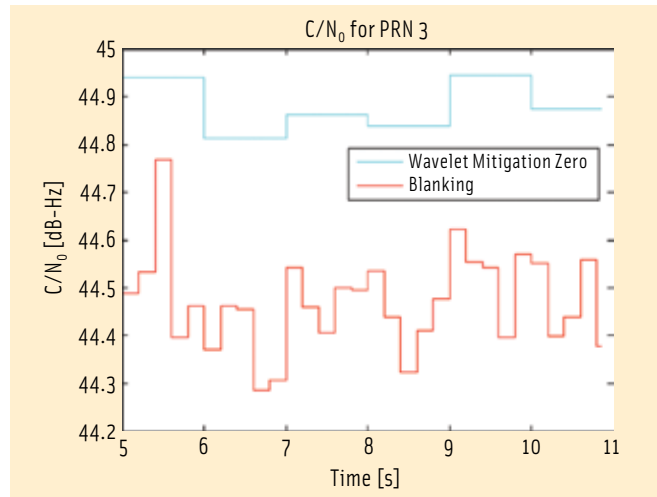


FIGURE 15 C/N0 effective estimation for PRN 3 – Wavelet mitigation versus blanking

the method of continuously monitoring the gain factor and steering the blanking within the front-end is not possible.

In order to compare both approaches, the AGC is modeled by monitoring the standard deviation of the discrete IF samples. The time interval for which the standard deviation is calculated is a key parameter of this approach.

In order to assure that the variance is calculated for a time period that is contaminated completely by the pulse, the time interval should not exceed half the pulse duration. We assess the performance for the E6 long pulses (0.2 millisecond pulse duration and 300 pps pulse repetition rate) at high power. The standard deviation of the IF samples for a time period of 20 milliseconds are shown in **Figure 14** where the six identified pulses are highlighted.

After identifying the pulses based on the AGC modeled via the standard deviation of the IF samples, we blank out the affected time intervals. **Figure 15** presents the resulting effective C/N_0 compared against the results obtained via wavelet-based interference mitigation.

A comparison of pulse blanking via IF sample standard deviation monitoring versus wavelet-based interference mitigation with respect to DLL, PLL, and FLL loop performance is shown in **Table 5**.

Summary of Wavelet-Based Interference Mitigation

We consider signal analysis by means of wavelets as an innovative technique, providing not only insight into the frequency content of the signal as with the traditional Fourier analysis but also enabling signal analysis in the time domain.

This technique allows a combined time-frequency analysis of the signal, which is highly desirable for pulsed interference. As many different wavelet basis functions exist, we can fine-tune our mitigation technique with respect to the expected interference.

Compared to traditional pulse blanking accompanied by monitoring of the analog AGC evolution, the wavelet transformation technique can detect a pulse with much higher precision. Moreover, by applying this technique the signal processing within the receiver does not suffer from potentially high recovery times after detection of a pulse.

Notch Filtering for CW Interference Mitigation

The design of interference mitigation algorithms applicable to continuous wave (CW) interference focuses on suppression of the high spectral peaks related to the interferer. **Figure 18** shows the power spectral density (PSD) of IF samples contaminated with CW interference.

We can describe a notch filter as one that passes all frequencies except those

	Pulse Blanking via AGC Modeling	Wavelet Mitigation Zero
DLL [m]	2.37e-1	2.29e-1
PLL [cycle]	3.53e-3	3.37e-3
FLL [Hz]	2.31	2.17

TABLE 5. Standard deviation of FLL, PLL and FLL errors

contained within a stopband bandwidth, BW , centered at the notch filter's center frequency F_{notch} . We define the stopband as those limits where the amplitude decreases by at least three decibels. The amplitude response of a notch filter is flat at all frequencies except for the stopband on either side of the centre frequency.

To specify a notch filter sampling frequency, F_s , the parameters to be defined include F_{notch} , BW , and a passband ripple, A_{pass} , as shown in the **Figure 16**.

Figure 17 illustrates the notch filter-based interference mitigation approach for continuous wave interferers, which we will now describe in greater detail.

Step 1 – Spectral Monitoring. We first estimate the continuous wave's center frequencies. (This method is not limited to a single CW interferer but can be applied to multiple CW interferers as well.) We then apply an FFT or estimate the PSD, while continuously monitoring the spectrum to adjust the filtering parameters appropriately.

Step 2 – Notch Filter Design. We determine the notch filter parameters and set

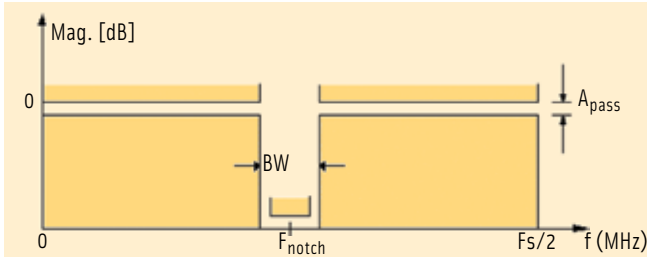


FIGURE 16 Notch filter design parameters

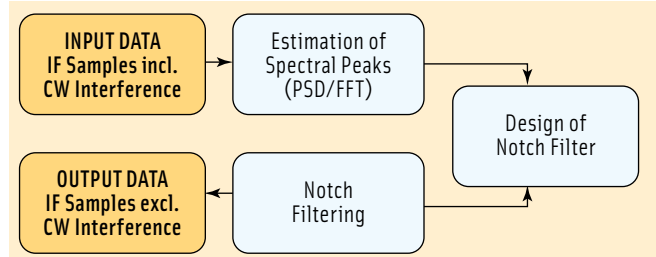


FIGURE 17 Notch filter interference mitigation process

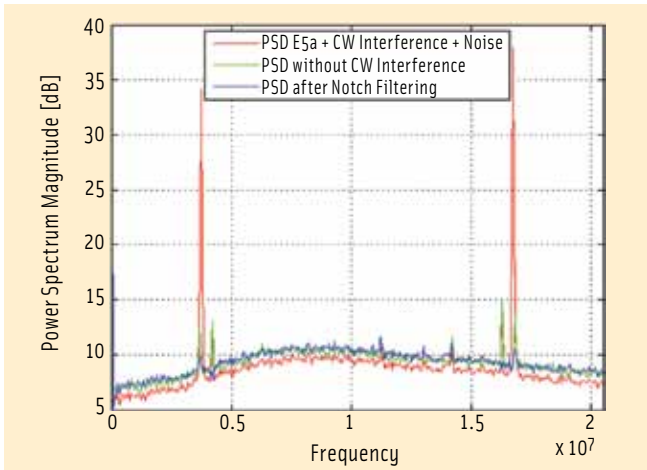


FIGURE 18 Power spectral density of the IF samples containing continuous wave interference

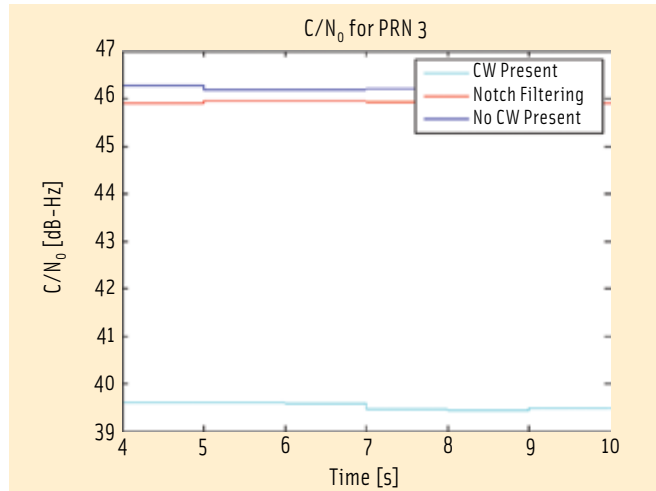


FIGURE 19 C/N0 effective estimation for PRN 3 - CW Interference

up the filter. Based on the information of the estimated interferer’s signal power, we can adjust the depth of the notch.

Step 3 – Notch Filtering. Notch filtering is carried out as part of the third and final step.

Performance Assessment of Notch Filtering–Based Mitigation Technique

Table 6 describes the scenario used in the application of the notch filter. A comparison of PSDs reflecting the effect of the notch filter for CW-interfered GNSS signals is given in Figure 18 based on the scenario described in Table 6.

After applying the notch filter, the spectral peaks originating from the CW interference were well suppressed. The resulting PSD is almost identical to the one without any interference.

Additionally, the estimated effective C/N_0 for PRN3 shown in Figure 19 clearly illustrates the effectiveness of the notch filter against CW interference. In this case, the effective C/N_0 drops from 46.2 dB-Hz to 39.5 dB-Hz in the

presence of CW interference and recovers to 45.9 dB-Hz after we apply notch filtering.

The performance benefits derived from Notch filtering counteracts CW interference in terms of DLL, PLL, and FLL errors are summarized in Table 7.

Conclusion and Future Developments

We have outlined two different interference mitigation approaches, applied to the digital part of GNSS receivers. Wavelet-based pulsed interference mitigation shows a significant potential for future use for both high- and low-power pulses, enabling accurate detection and mitigation. Significant performance improvements are measured at both the C/N_0 level and tracking loop level have been reported for high power pulsed interference.

Additionally, our analysis of notch filtering against CW interference threats indicates significant capabilities as well.

We should underline that all algorithms have been implemented in the

Desired signal	Galileo E5a (BPSK(10))
Coherent integration time	1 ms
Loop bandwidths	DLL: 5 Hz PLL: 10 Hz FLL: 4 Hz
RF front-end bandwidth	13 MHz (double sided)
CW interference	1/5 ratio: 31.6 dB Doppler offset for PRN3: 90.2 Hz

TABLE 6. Scenario characterization for high-power pulsed interference

	No CW	CW Present	Notch Filtering
DLL [m]	1.50e-2	8.64e-2	1.77e-2
PLL [cycle]	3.13e-3	9.47e-3	2.90e-3
FLL [Hz]	9.18	5.08e1	9.75

TABLE 7. Standard deviation of DLL, PLL, and FLL errors

IpexSR software receiver, enabling interference mitigation in a post-processing laboratory environment. Currently, implementation of the wavelet-based interference mitigation approach for real-time applications in particular is being

pursued at the University FAF Munich Institute of Geodesy and Navigation.

Acknowledgment

The results shown in this paper have been accomplished at the Institute of Geodesy and Navigation of the University FAF Munich within ESA contract No. 21095/07/NL/HE.

Additional Resources

[1] Anyaegbu, E., and G. Brodin, J. Cooper, E. Aguado, and S. Boussakta, "An Integrated Pulsed Interference Mitigation for GNSS Receivers," *Journal of Navigation*, The Royal Institute of Navigation, Cambridge University Press, Volume 61, Issue 2, 2008

[2] Burrus, C.S., and R. A. Gopinath and H. Guo, *Introduction to Wavelets and Wavelet Transforms: A Primer*, Prentice Hall, Upper Saddle River, New Jersey, USA, 1998

[3] ICAO NSP WG162/WP5: Interference Susceptibilities of Aeronautical Systems Operating in the 960-1215 MHz Band, 2005

[4] Steingass, A., and A. Hornbostel and H. Denks, "Airborne Measurements of DME Interferers at the European Hotspot," *Proceedings of European Navigation Conference ENC/GNSS 2009*, Naples, Italy, May 04, 2009

[5] Stöber, C., and M. Anghileri, A. Sicramaz Ayaz, D. Dötterböck, I. Krämer, V. Kropp, J.H. Won, B. Eissfeller, D. Sandromà Güixens, and T. Pany, "IpxSR: A Real-Time Multi-Frequency Software GNSS Receiver," *Proceedings of IEEE ELMAR 2010*, Zadar, Croatia

Authors



Guenter W. Hein is head of the Galileo Operations and Evolution Department of the European Space Agency. Previously, he was a full professor and director of the Institute of Geodesy and Navigation at the University FAF Munich. In 2002 he received the prestigious Johannes Kepler Award from the U.S. Institute of Navigation (ION) for "sustained and significant contributions to satellite navigation." He is one of the CBOC inventors.



Matteo Paonni is a research associate at the Institute of Geodesy and Navigation at the University of the Federal Armed Forces Munich, Germany. He received

his M.S. in electrical engineering from the University of Perugia, Italy. He is involved in several European projects that focus on GNSS. His main areas of interest are GNSS signal structure, GNSS interoperability and compatibility, and GNSS performance assessment.



Jaegyung Jang received B.S and M.S degrees and a Ph.D. in aerospace engineering at Seoul National University. He joined the Institute of Geodesy and Navigation, University of FAF in Munich in 2007. Before moving to Munich he worked at Samsung Electronics as senior research engineer. His research interests during the Ph.D. studies were mainly attitude determination algorithms and receiver development. In Munich he was involved in research about future navigation system design and interference mitigation techniques as software receiver team's member. He currently works as a chief GPS research engineer in the mobile electronics industry.



Bernd Eissfeller is a full professor of navigation and since 2008 director of the Institute of Geodesy and Navigation at the University of the Federal Armed Forces in Munich. He is responsible for teaching and research in navigation and signal processing. Until the end of 1993 he worked in industry as a project manager on the development of GPS/INS navigation systems. He received the Habilitation (venia legendi) in navigation and physical geodesy, and from 1994-2000 he was head of the GNSS Laboratory of the Institute of Geodesy and Navigation. Eissfeller is the author of more than 215 scientific and technical papers.



Stefan Wallner studied at the Technical University of Munich and graduated with a Diploma in techno-mathematics. From 2003 to 2010 he was a research associate at the Institute of Geodesy and Navigation at the University of the Federal Armed Forces Germany in Munich. Since 2010 he has been working as a GNSS system analysis engineer at the European Space Agency/ESTEC in Noordwijk, The Netherlands, in the field of Galileo evolution, GNSS standardization, and RNSS compatibility. His main topics of interests can be denoted as GNSS spreading codes, the signal structure of Galileo, and RF compatibility of GNSS.



José-Ángel Ávila-Rodríguez is since March 2010 GNSS signal and receiver engineer of the Galileo Evolution Team at ESA/ESTEC. Between 2003 and 2010 he was research associate at the Institute of Geodesy and Navigation at the University of the Federal Armed Forces Munich. He was awarded the Bradford Parkinson prize in 2008 and the following year he received the Early Achievement Award, both from the U.S. Institute of Navigation.



Jaron Samson is a radio-navigation system engineer at the European Space Agency (ESTEC/The Netherlands). He has been involved in several projects for EGNOS, Galileo, and GNSS Evolutions. He received his M.Sc. degree in geodesy from Delft University of Technology, The Netherlands.



Francisco Amarillo Fernández received his Master's Degree in telecommunication engineering at the Polytechnic University of Madrid (UPM). Since 1998 he has been working on the design and development of GNSS systems. In 2001 he joined the European Space Agency (ESA) Technical Directorate, and since then he has worked for the Galileo program and leads numerous research activities in the field of GNSS evolutions. IG